Numerical Analysis of BVI Noise Reduction Using Active Flap Control

Choongmo YANG, Takashi AOYAMA, and Shigeru SAITO
Japan Aerospace Exploration Agency (JAXA), Tokyo, Japan

ABSTRACT

The effect of geometric position of the active flap is examined to reduce the blade vortex interaction (BVI) noise of helicopter. For the better understanding of the different mechanism of noise reduction, variation of phase of Active Flap Control (AFC) is also applied according to the flap position on the blade. A moving overlapped grid system is used with three types of grid including rotor grid, inner background grid and outer background grid for helicopter flight simulation. The rotor grid communicates with inner-/outer-background grids during unsteady computations. The BVI noise of rotor is predicted using a combination method of an unsteady Euler code with an aeroacoustic code based on the Ffowcs-Williams and Hawkings formulation. As the results, the effect of flap position on BVI noise is quantitatively predicted to show that the flap near tip region is more effective to achieve BVI noise reduction in the condition of well-adjusted phase.

1. INTRODUCTION

1.1 Active control to reduce BVI noise of helicopter

Blade-vortex interaction (BVI) is one of the main noise sources of helicopters. Various kinds of reduction techniques for BVI noise have been proposed. One of them is flight path management and control. Schmitz, et al.[1,2] developed a quasi-static acoustic mapping (Q-SAM) method to estimate ground noise level trends and indicated that choice of flight path angle, X-Force, and vehicle acceleration has an important influence on the ground noise exposure. Alternative techniques are passive tip-shape modification[3-6] and active rotor control[7]. The tip-shape modification has been successfully applied for the reduction of high-speed impulsive (HSI) noise[8,9], which is generated by the shock wave on advancing blade surface. However, the reduction of BVI noise by this technique is not expected much. Therefore, active rotor controls such as higher harmonic control (HHC), conventional individual blade control (IBC), tip jet blowing, active tab control (ATC), active twist rotor (ATR), and active flap control (AFC), are expected to become a breakthrough for significant reduction of BVI noise.

Recently, flight tests have confirmed the feasibility of closed loop IBC for vibration reduction[10]. ATC was originally devised by JAXA (Japan Aerospace Exploration Agency) and Kawada Industries, Inc. and its effect on BVI noise reduction is shown by wind tunnel tests[11,12] and numerical analysis[13]. A joint team of ONERA and DLR has been investigating two active twist concepts, Active Twist Blade (ATB) and Twistable Section Closed by Actuation (TWISCA), in the project called “Active Twist Blade” (ATB)[14]. Closed-loop vibration control tests[15] produced simultaneous reduction of both 4P and 1P hub normal shears in the NASA/Army/MIT Active Twist Rotor (ATR) program. The integration of piezoelectric actuator packs and a robust power bus concept into a full scale blade was demonstrated by Boeing’s full-scale active blade section[16], and acoustic aspects of ATR are also discussed[17].

Although there are structural discontinuities in actively controlled flap, it has advantage in several factors[18] compared to other active techniques: (1) low power consumption for actuation than HHC or classical IBC, (2) relative simplicity of implementation, and (3) independence of helicopter’s primary control system. Simultaneous reduction of noise and vibration by AFC has been demonstrated by simulations[19,20]. Furthermore, the multidisciplinary nature of rotorcraft offers many opportunities for the applications of active techniques. AFC has a potential to enhance not only rotor performance[21] but also active interrogation rotor fault detection and diagnostic system[22] that employs trailing-edge flaps as actuators is investigated.

The Advanced Technology Institute of Commuter-helicopter, Ltd. (ATIC), which had been temporarily funded by the Japanese government from 1994 to 2001, conducted a whirl tower test[23, 24] of full-scale rotor with active flap at the last of their research activity in 2000. A package of an electromagnetic actuator and trailing-edge flap called Heliflap[25] was tested in another full-scale whirl testing and its capability to provide high amplitude flap deflections at high frequencies while requiring reasonable power and without heat dissipation problems was demonstrated. ONERA and DLR studied on the optimization of flap position and deflection laws using their numerical tools and concluded that several independent flaps were required for simultaneous reduction of noise and vibration because the optimum flap position in span-wise direction differs depending on the objective of noise and vibration reductions[26]. A full scale blade with AFC system[27] was designed based on this finding and its reliability under high centrifugal force and blade loads was confirmed on a whirl tower. Various activities on AFC in Germany and France are

reviewed in Ref. 28. Boeing released a piece of news in May 2004 on their web site[29] that the Smart Material Actuated Rotor Technology (SMART) system with active flap was successfully tested on a whirl tower in a joint program with DARPA, NASA, the U.S. Army, and three universities. An open and closed loop wind tunnel testing[30] in the Glenn L. Martin wind tunnel at the University of Maryland successfully indicated that a Mach-scaled active rotor system with piezoelectric bender actuated trailing-edge flaps reduces vibration.

1.2 Active Flap Control (AFC) methods

Several efforts have been devoted to develop comprehensive aeroelastic modeling for rotors with AFC[31]. In these efforts, unsteady aerodynamics of AFC is represented by relatively simple models such as a method[32] including indicial-based flap unsteady aerodynamics[33] and a pseudo-implicit free wake model[34] or a method[35] based on a rational function approximation (RAF) because their main concern is the elasticity caused by AFC. However, more accurate modeling for the unsteady aerodynamics of AFC is required when BVI noise is mainly concerned because the effect of AFC on the trajectory and structure of tip vortex should be accurately taken into account.

The authors applied a CFD code using moving overlapped method, which is one of the most advanced techniques for tip-vortex capturing at present, to obtain better understandings for the effect of AFC on noise reduction[36]. Based on the understanding of the relation between flap motion and vortex vertical position, the authors proposed a simple model to clearly comprehend the effect of flap phase angle on BVI noise of one-bladed rotor. In this model, it was assumed that the intensity of BVI noise is dominated by the 2D BVI at the intersectional plane including effective noise source, and the change of core radius and circulation due to the blade flapping motion was neglected because the noise intensity is considered to be dominated by miss-distance. Figures 1 a)-d) classifies the typical type of 2D BVI into Types I, II, III, and IV. The left-hand side figure in Fig. 1a) illustrates the geometrical relation between an airfoil and vortices shed from a preceding blade with active flap in A<d0, where A is the vertical distance between the uppermost and neutral positions of vortex and d0 is the miss-distance between the airfoil and the vortex shed from a blade with active flap of neutral position. The prediction of the effect of flap phase angle on BVI noise was explained by understanding simple model derived from this research.

1.3 Geometric effect of AFC

As the next important parameter of AFC, the effect of geometric position of the AFC is examined in the present paper. By varying the flap position as well as phase angle, we can understand the mechanism of AFC on BVI noise, and approach the optimal condition of AFC. The span-wise length and chord-wise length are fixed for simplicity, and the frequency and amplitude of flap motion are also invariant during calculation. The general idea that active flap near tip is more effective to reduce BVI noise is verified, and the change by inward flap (to root) is also discussed.

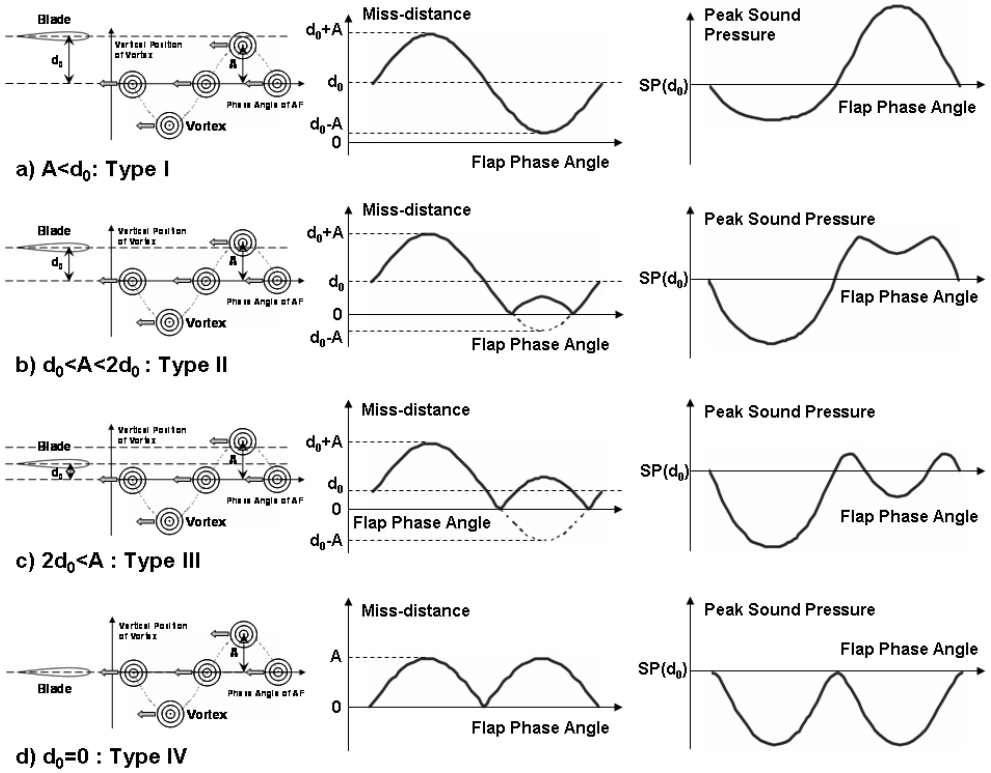

Fig 1: Classification of 2D BVI type

2. NUMERICAL METHODS

2.1 Overlapped Grid System

A moving overlapped grid system with three different types of grids (rotor grid, inner and outer background grids) is used to simulate BVI of helicopter. Figure 2 shows a perspective view of grid system for the whole computational domain of grid system to solve full helicopter configuration[37]. The inner background grid is placed around the rotor disk. The outer background grid covers the whole computation region with a sparse grid density. The body-fitted blade grid in O-H topology, as shown in Fig 3, moves according to the blade motion such as rotation, flapping, feathering, and lagging. Active flap, which is located at the specified geometric position, oscillates according to the phase, frequency, and amplitude of flap motion.

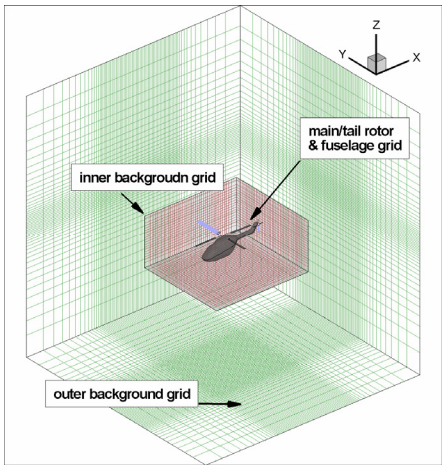

Fig.2: Perspective view of grid system

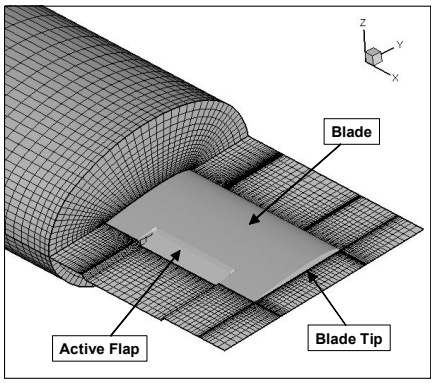

Fig.3: Perspective view of blade with active flap

Table 1 shows the specification of each grid in the case of 1-blade rotor for AFC calculation. Most of the grid is concentrated in inner-background grid, which captures the trace of tip vortex during several rotations around rotor rotating plane. The number of grid points in span-wise direction is considerably increased to match the grid density of the blade grid with that of the inner background grid. For the validation using 2-blade rotor, same background grids are used with similar grid points for blade grid.

The airfoil model of main-rotor blade comes from AH1-OLS blade[38] (modified BHT 540), which has been used for the aerodynamic and noise testing by NASA. The characteristics of OLS rotor with 1.916m diameter (6.6ft) are shown in Fig. 4. The aspect ratio of main-rotor is 9.21.

Table 1: Specifications of grid systems

Inner background grid	(X×Y×Z) 450×400×80 = 14,400,000
Outer background grid	(X×Y×Z) 83×79×49 = 321,293
Blade grid	(chord×normal×span) × blade (83×25×131) × 1 = 271,825
Total	~15,000,000 points
Inner background spacing	0.05c (=0.006*R*)

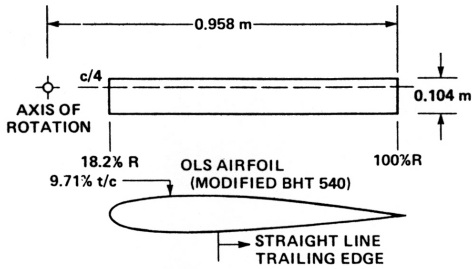

Fig.4: Geometric dimension of OLS model rotor

2.2 Aerodynamics

A three-dimensional numerical flow solver for the compressible Euler equation is used to analyze the detailed behavior of tip vortex.

For the calculation of blade grid, inviscid flux vectors are separated using Roe's flux difference splitting (FDS) algorithm, with third-order accuracy using a TVD scheme. For the time integration, second-order Euler backward scheme is used in the conventional delta form. A diagonalized ADI method with an upwind flux-split technique is used in the linearized implicit part for the discretionary governing equations. A detailed derivation of the governing equation and numerical schemes is described in a previous work by Aoyama et al.[39] The typical dividing number along the azimuthal direction is about 4800 per revolution, which corresponds to the azimuthal angle about 0.075˚. The unsteady calculation is impulsively started from 0˚azimuth angle.

For the calculations over background grid, the flux difference across cell interface is divided also using a compact TVD scheme[40] to get third order accuracy. MUSCL cell interface value is modified to achieve 4th-order high accuracy in the background Cartesian grid. Simple High-resolution Upwind Scheme (SHUS)[41] is employed to obtain numerical flux. SHUS is one of the Advection Upstream Splitting Method (AUSM) type approximate Riemann solvers and has small numerical diffusion. The four stage Runge-Kutta method is used for

the present calculation. The free stream condition is applied for the outer boundary of the outer background grid.

Calculations are performed using Central Numerical Simulation System (CeNSS), the main part of the third-generation numerical simulator of JAXA. It is composed of high performance UNIX servers, FUJITSU PRIMEPOWERs, which are connected by a crossbar network. CeNSS has 9TFLOPS peak performance, 3TB memory, 50TB disk storage, and 600TB tape archive.

2.3 Aero-acoustics

The prediction method of the far field acoustic pressure is based on the combination of CFD technique with an acoustic equation solver. Although direct computation can be used to get the noise solution directly from the flow calculation with CFD based methods, this is available only in the near field in spite of huge computing cost. At present, the best way is the coupling with the integral method for far-field prediction. Acoustic analogy, which is re-arranged into the Ffowcs Williams-Hawkings Equation, is widely used and still under construction for better applications. Retarded time solution to the Ffowcs-Williams and Hawkings equation, neglecting quadruple noise, can be written in the form of Formulation1 by Farassat[42]. The prediction of rotor noise is conducted in the following procedures: 1) calculation of sound pressure of the noise source, 2) acoustic prediction computation at the observer position, and 3) post-processing of the noise data in the way of sound level using visualization or audible converting.

Hypothesis of the Ffowcs-Williams and Hawkings equation[43] to be satisfied are known that the noise source must lay in low speed flow, and the observer should be located outside of the source region (i.e. outside of the boundary layer, separation flow or wake) in order to avoid the nonlinear effect. In most calculations to compare the results with wind tunnel experiment, the observer moves in the same direction and at the same speed as the noise source. The pressure distribution on the blade surface calculated by the CFD code is stored every 0.5 degrees in azimuth-wise direction as the input data in noise calculation.

3. VALIDATION

3.1 Validation of BVI noise analysis

Numerical computations are performed by the original code and the results are compared to an experimental data[38] of BVI noise radiated from a 1/7-scale model rotor of AH-1 series helicopter and to another calculation result[44]. One of the testing conditions (see Table 2) is chosen to evaluate the capability of our original code for the prediction of BVI noise without AFC. Figures 6 show the measured and calculated time histories of sound pressure at the microphone positions indicated in Fig. 5. CFD results by Strawn et al. are shown by the grey lines. They directly applied the trim condition indicated by "Strawn" in Table 3 to obtain the acoustic signals without iteratively adjusting the trim condition to the experimental thrust value with zero rolling moments across the rotor disk. While the positive spikes observed in the experimental data (dotted lines), which are caused by the interactions between blades and vortices, are not clearly captured by their method in both microphone positions, the predictions are fairly improved by the present method using the same trim condition as indicated by the red line. If the trim condition calculated by CAMRADII (Comprehensive Analytical Code for Rotorcraft Aerodynamics and Dynamics) shown in Table 3 is applied to the present method, the improvement becomes more remarkable except for the over- predictions of the first negative and positive peaks at Mic. 3 as indicated by the blue line. Therefore, the prediction of BVI noise is strongly affected by the trim data. There are several reasons for the discrepancies between the experimental data and our predictions such as the lack of accuracy in calculated trim condition, numerical scheme, and the interpolation used in the overlapped grid method, the neglect of viscosity and blade elasticity, and the lack of grid number. However, it is at least confirmed that our method successfully captures the distinct spikes of BVI noise according to the discussion here.

Table 2: Operating conditions

Thrust Coefficient, C_T	0.0054
Tip Mach Number, M_T	0.664
Advance ratio, μ	0.164
Tip path plane angle	1.0˚ (aft.)

Table 3: Trim conditions

	Strawn	CAMRAD II
Collective pitch angle	6.14˚	5.73˚
Lateral Cyclic pitch angle	0.9˚	0.97˚
Longitudinal Cyclic pitch angle	1.39˚	1.86˚

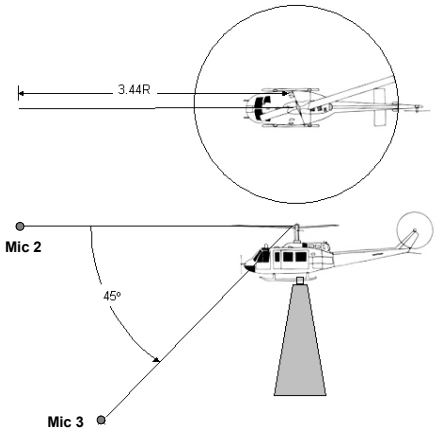

Fig. 5: Microphone position

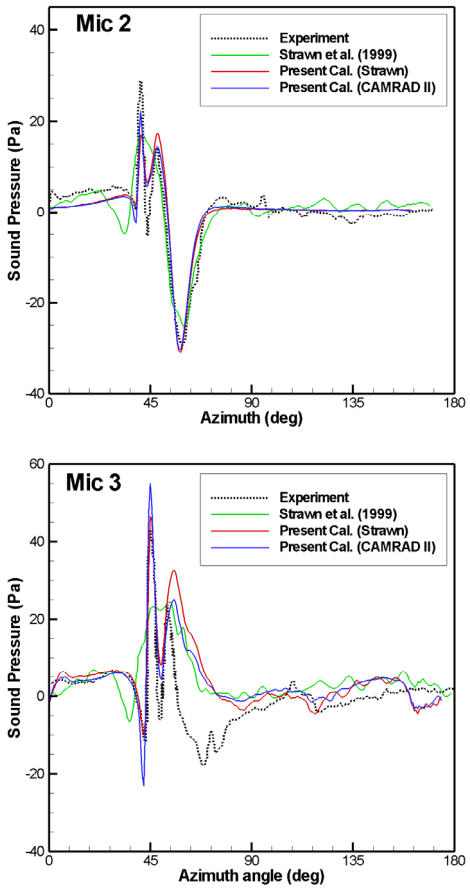

Fig. 6: Comparison of sound pressures between calculations and measurement at microphone position

3.2 Validation of AFC noise analysis

The numerical code has been extended for the analysis of active flap control, and calculations are performed to demonstrate the capability of the present code for capturing the effect of AFC on blade aerodynamics. The characteristics of blade and active flap and the operating condition are shown in Table 4. The pitch angle of active flap, $\theta_{AFC}(\psi)$, is defined in the Fig. 7, where ψ, θ_{0AFC}, P_{AFC}, and ψ_{AFC} are the azimuth angle of blade, the amplitude, frequency, and phase angle of active flap control, respectively.

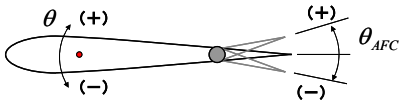

$$\theta_{AFC}(\psi) = \theta_{0AFC} \cos P_{AFC}(\psi - \psi_{AFC})$$

Fig 7: Pitch angle of active flap

Not only vortices from blade tip, but also vortices from inner and outer edges of active flap are generated according to the flap motion. When the active flap is located at the lowermost position, all of the three vortices become stronger due to the high blade lift. Even the vortices shed from the flap edges become stronger owing to flap angle higher than blade pitch, considering the increasing inflow Mach number along span by the rotation of blade, the vortex from blade tip is supposed to be the strongest. Basically, the motion of active flap affects tip vortex in two different ways. One of them is that the extra lift generated by the deflection of flap directly changes tip vortex. The other is that the modification of pitching moment on a blade section generated by the aero-elastic deflection of flap changes the blade section angle of attack resulting in the change of tip vortex. The model blade calculated here is assumed to be stiff in torsion. Therefore, only the former effect of active flap on tip vortex is considered here.

Calculated results of the present method are compared to the experimental data[45] of one-bladed rotor with active flap obtained by ATIC in 1997. The schematic of the model rotor is illustrated in Fig. 8. The blade is fixed to the rotor hub rigidly and only the blade pitching motion is allowed. The details of the drive mechanism of AFC are described in ref. 45.

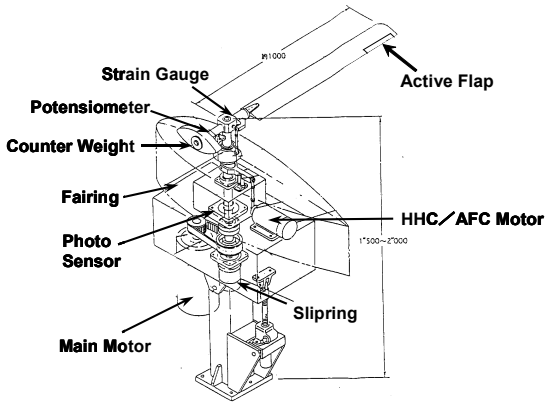

Fig. 8: Schematic of model rotor

Table 4: Model rotor and operating condition

Blade	
Hub type	rigid in flap and lead-lag
Rotor radius	1m
Blade chord length	0.12m
Airfoil	NACA0012
Twist angle	0.0°
Planform	rectangular
Number of blade	1
Active Flap	
Chord -wise length	0.25*c*
Span-wise length	0.18*R*
Span-wise position	0.80-0.98*R*
Amplitude	6.0°
Frequency	2 per rotor revolution
Operating Condition	
Free-stream velocity	20.1m/s
Rotor rpm	600
Collective pitch angle	5.0°
Cyclic pitch angle	0.0°
Shaft tilt angle	0.0°
where *c*: blade chord *R*: rotor radius	

Figure 9 compares measured and calculated sound pressure in three cases, without active flap control (w/o AFC), with 50˚and 170˚of phase angles. Each of the blue and red lines has the offset of ±20˚, respectively, in order to make the comparison easy. The microphone is located beneath the rotor disk as indicated by the red point in Fig. 10. The gentle hill observed just after the positive peak in the calculated result is caused by the near field loading noise because the distance between the noise source and the observer position is short and it disappears at the far field observer position. The predicted positive peak value in the case of w/o AFC and the effect of flap phase angle on the positive peak are accurately captured. Therefore, it is confirmed that the present CFD code has the capability of reasonably predicting the effect of AFC on BVI noise.

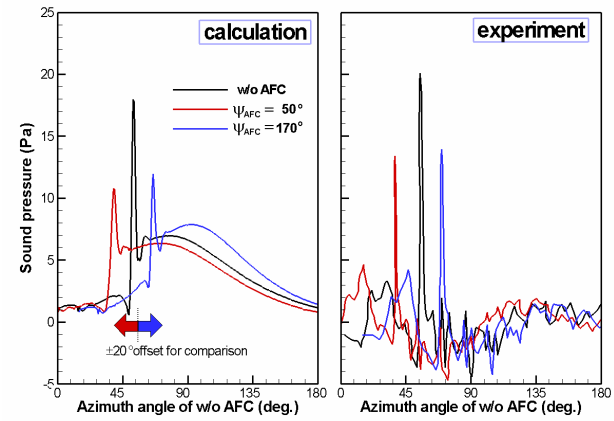

Fig. 9: Comparison of measured and calculated sound pressure

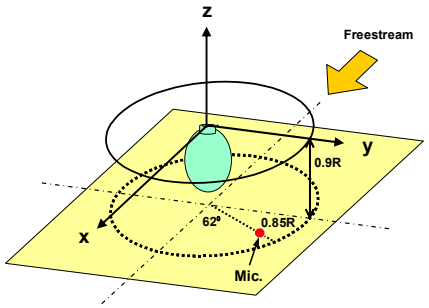

Fig. 10: Microphone position

4. RESULTS AND DISCUSSIONS

4.1 Theoretical and calculated analysis

The effect of geometric position of active flap in span-wise direction is calculated using the same model rotor and operating condition. It is the continuing research of AFC which was mentioned in the Introduction. The model rotor and operating condition is the same as those of validation in previous section. Span-wise position of beginning of active flap with a span-length of 0.18*R* varies from 0.40*R* to 0.8*R*, as shown in Fig.11. The calculation cases are expressed to be 0.4-0.58*R*, 0.5-0.68*R*, 0.6-0.78*R*, 0.7-0.88*R*, and 0.8-0.98*R*.

Figure 12 shows the diagram of vortex generation according to flap motion. As flap oscillating, the change of sectional lift of flap region also produces the oscillating overall lift of blade itself. Not only the strength of tip vortex, which is strongly related to the blade lift, but also the vertical position of vortex center have oscillating motion. As concerned to BVI noise, miss-distance, the vertical distance of tip vortex from leading edge when BVI occurs, can be one of importance factors. The primary role of AFC is thought to be the change of the characteristics of tip vortex by interfering the sectional lift and overall lift in the end. The secondary effect of active flap is related to the flap vortex from both sides of flap edge, which has opposite rotating direction. Compared to the tip vortex from blade tip, these flap vortices have relatively small magnitude. The effect of flap vortex will be discussed in the next session.

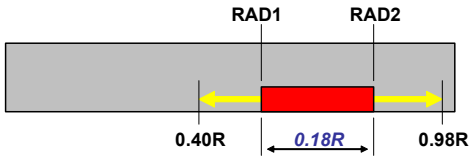

Fig 11: Variation of span-wise position of active flap

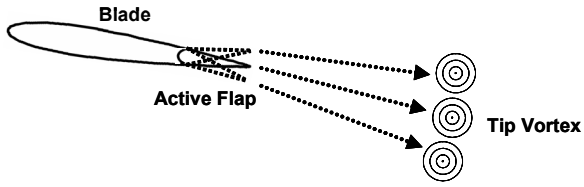

Fig 12: Generation of tip vortex according to flap motion

One of the most important models is the relation between miss-distance and noise intensity. It can be assumed when the variation of peak sound pressure is drawn

$$SP(d) = \frac{kSP(0)}{d^2 + k},$$

where SP is peak sound pressure as a function of miss-distance, d, and k is a constant. Figure 13 indicates the relation between miss-distance and peak sound pressure in the three cases. The detail derivation of this equation and graph are explained in the previous research[36]. From this relation, we can predict the relation between flap motion and peak sound pressure directly with the hypothesis that miss-distance of tip vortex is proportional to blade lift.

A simple model for the lift of blade with AFC can be derived from the geometric relation and flap motion by integrating the sectional lift along blade span. Sectional lift is calculated by 2D blade element theory using free-stream Mach number, azimuth angle, flap configuration and flap operating condition, where the effect of flap is partially evaluated using proper weighting function. Figure 14 shows the variations of theoretical and calculated lifts with AFC according to flap phase

angle, 0˚, 60˚ and 120˚ as a function of azimuth angle when flap is located at 0.65-0.83*R* as a sample condition.

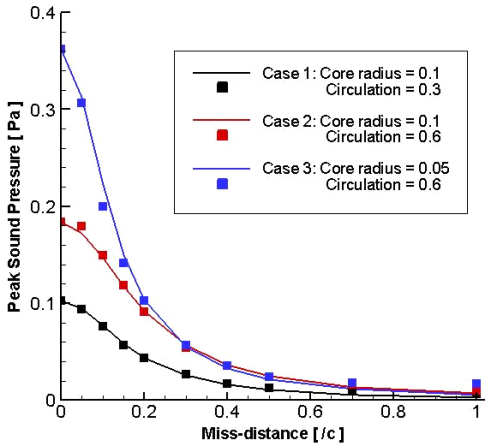

Fig. 13: Relation between miss-distance and peak sound pressure

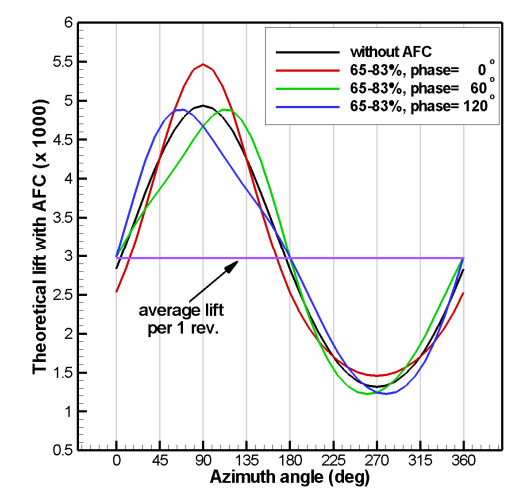

(a) theoretical lift

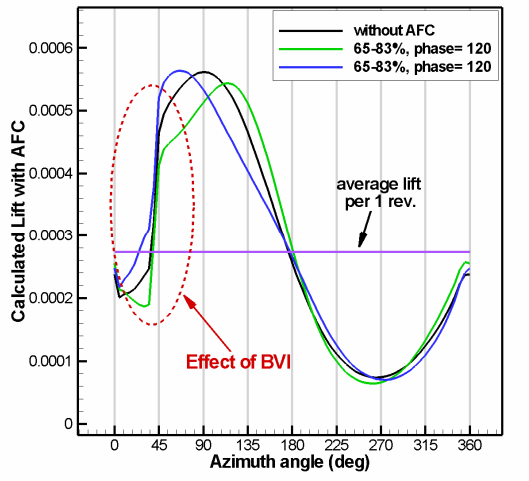

(b) calculated lift

Fig. 14: Variation of theoretical and calculated lift with AFC according to flap phase angle as a function of azimuth angle.

Compared to the theoretical lift, calculated ones shows good agreement in the tendency of lift change by the flap motion. Calculated results also show the effect of BVI around 45˚ of azimuth angle.

Figure 15 shows the diagram of trajectory of tip vortex, where the red points correspond to the phase angles from 180˚ to 360˚ with 45˚ in turns. The vertical plane is parallel to the free-stream direction. This plane and the leading-edge line of the blade at the azimuth angle of around 45˚ cross each other at the blade span-wise position of 0.9*R*, where the effective source of BVI noise is assumed to be located. In addition, the bow-shaped tip vortex begins to interact with the blade at around tip and mid-span simultaneously, which implies that two peaks of $\partial p/\partial t$ on blade surface in tip and mid-span regions at each azimuth position are expected to be revealed in noise analysis. The azimuth angle of vortex generation, ψ_{VG} , in Fig. 15 is where the tip vortex which interacts with the blade at the position of effective source is generated at the trailing-edge of blade tip end. It corresponds to about 143˚ in the present flow condition.

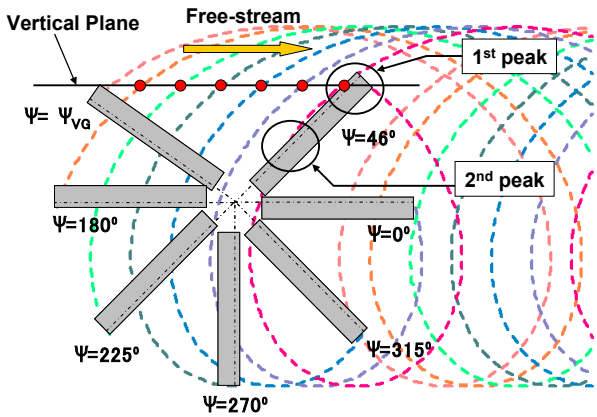

Fig. 15: Trajectory of tip vortex

The time-wise variation of vortex location In Fig. 15 is simple because the vortex is not disturbed by any other blades during its convection from its generation to the blade vortex interaction. The vertical position of vortex at the BVI event obviously shifts as the change of flap phase angle, that is, the change of flap angle in the way of altering the lift of blade as described in Fig. 14. If we consider the azimuth angle of vortex generation, 143˚ in Fig. 14, the effect of flap condition on blade lift can be easily estimated.

4.2 Vorticity Analysis

The traces of tip vortex and flap vortex along the can be examined by vorticity analysis along the plane shown in Fig. 15. Vorticity analysis demonstrates movement of both vortices and the change in the characteristics of vortex by flap conditions.

Figure 16 show the iso-surface and mid-section of vorticity at 0˚ azimuth angle according to the flap position

for the cases of flap phase 60˚ and 120˚ respectively. The mid-section fits the plane which is described in Fig. 15. The figures indicate that the flap vortex comes first and tip vortex follows with different miss-distance. And the strength of flap vortex is different according to the flap position and phase, but compared to the tip vortex, the strength of tip vortex is definitely larger than the one of flap vortex.

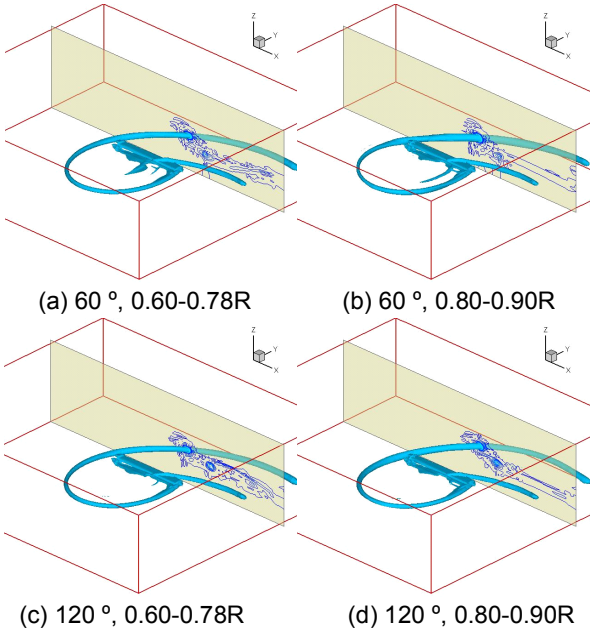

(a) 60 °, 0.60-0.78R (b) 60 °, 0.80-0.90R

(c) 120 °, 0.60-0.78R (d) 120 °, 0.80-0.90R

Fig. 16: Comparison of iso-surface and mid-section of vorticity at 0˚ azimuth angle according to the flap position and phase

Figures 17(a)-(d) show the time-wise variation of vorticity contour in a vertical plane shown in Fig. 15 in four cases, w/o AFC, phase angle of 60˚, 100˚, and 170˚, respectively. These contours present quite good understanding of the trace of tip vortex and the trace of flap vortex from the vortex generation to the BVI occurrence. The weak vortices along the red dashed arrow in Fig 17(a) represent the trace of flap vortex, and the strong vortices along black dashed arrow represent the trace tip vortex. The traces of flap vortex move downward when phase of flap shifts from 60˚ to 120˚ for both cases of flap at 0.80-0.90*R* and 0.60-0.78*R*. Compared to the dramatic change of tip vortex for the case of flap at 0.80-0.90*R*, the one at 0.60-0.78*R* seems not so much affect by flap. They also show the difference of miss-distances when BVI happens according to the flap condition. Compared to the small difference of miss-distance between flap phase of 60˚ and 120˚ for the case of 0.60-0.78*R*, the case of 0.80-0.98*R* show quite large movement of vortex centers to produce dramatic change in miss-distance.

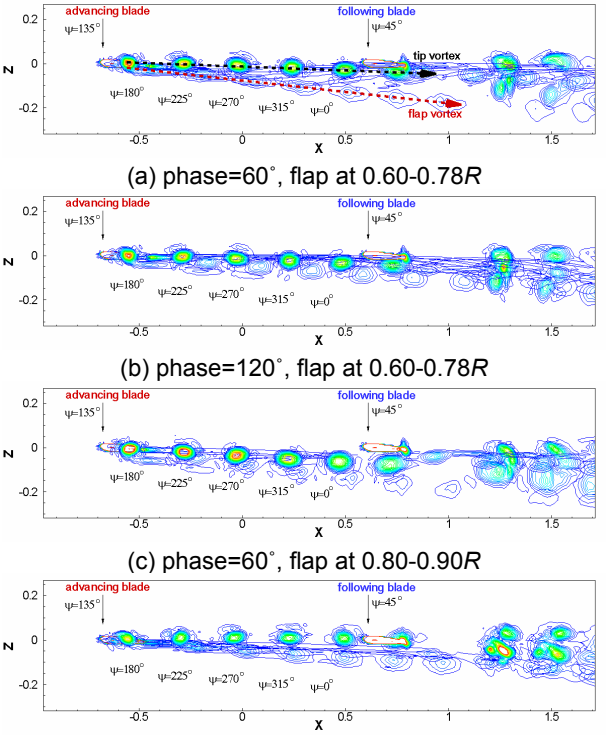

(a) phase=60˚, flap at 0.60-0.78*R*

(b) phase=120˚, flap at 0.60-0.78*R*

(c) phase=60˚, flap at 0.80-0.90*R*

(d) phase=120˚, flap at 0.80-0.90*R*

Figure 17: Comparison of vortex trace using vorticity contours at several azimuth angles according to the flap position and phase

Figure 18 shows the pressure carpet using span-wide line at 3% chord on upper/lower surface. It shows clearly the sudden change of surface pressure around 45˚ azimuth angle and 90% of span, which comes from the interaction with tip vortex and is converted to the BVI noise. The major difference according to the flap position occurs at the figures of lower surface for the range of azimuth angle from 0˚ to 45˚ around 90% of span, which is thought to come from the interaction with flap vortex. As flap moves outward from 0.4-0.58*R* to 0.7-0.88*R*, the pressure change, which appears as the change of color in contour, get larger and moves to the azimuth angle of 45˚, where BVI occurs. For the better understanding of the phenomena, unsteady pressure history at surface point of 3% chord and 90% span for one revolution with flap phase of 120˚ are shown in Fig. 19 and Fig. 20.

As a basic model, unsteady pressure history without AFC in Fig. 19 represents a typical BVI occurrence with the sudden pressure change during BVI. The time derivative of this unsteady pressure has good correlation with noise intensity and its maximum value appears at about 0.9*R* in the azimuth angle of 40˚.The interaction with flap vortex is supposed to occur just before BVI, which are shown in both Fig.16 and Fig.18.

Figure 20 shows the zoom-view of Fig. 19 for the azimuth angle from 0˚ to 45˚, which show the effect of interaction between blade and vortex including both tip vortex and flap vortex. Compared to case without AFC in

black line, all cases with AFC show local peak in unsteady pressure in opposite direction to the peak from tip vortex. As flap moves to outward (0.80-0.98*R*), the azimuth angle at peak from flap vortex approaches to the azimuth at peak from tip vortex, as shown by the yellow arrows in Fig. 20. These figures verified that the calculation captures successfully the interaction with flap vortex as well as tip vortex. Also the gradient of pressure changes by flap vortex is relatively small compared to that of tip vortex, which implies that interaction with flap vortex has insignificant effect on BVI noise itself. The actual noise calculated from these unsteady surface pressures will be discussed in the following session.

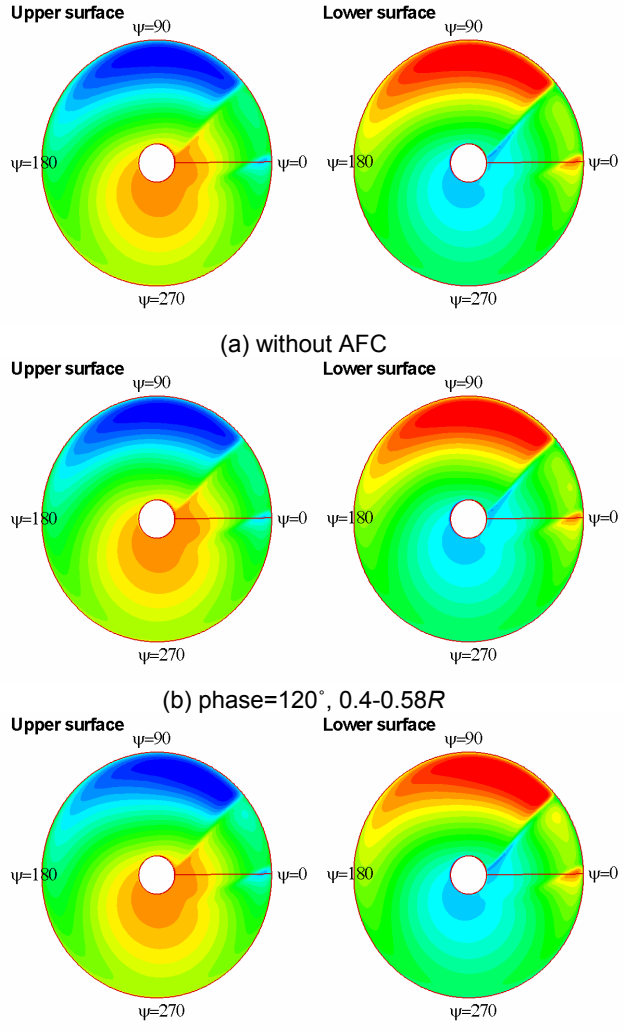

(a) without AFC

(b) phase=120˚, 0.4-0.58*R*

(c) phase=120˚, 0.7-0.88*R*

Fig. 18: Pressure carpet using span-wide line at 3% chord on upper/lower surface

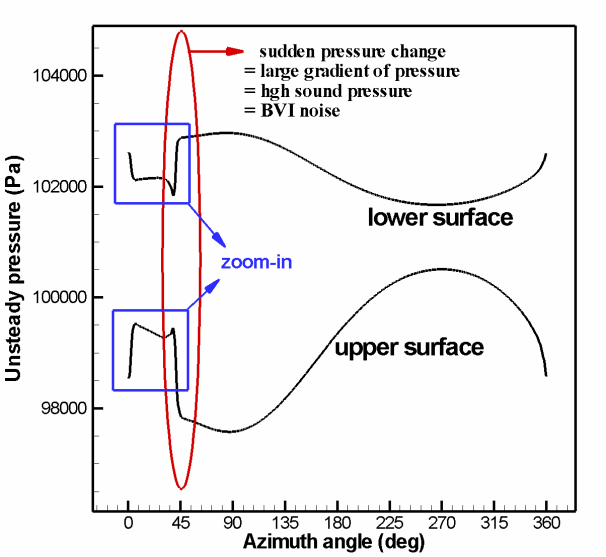

Fig 19: Unsteady pressure history at surface point of 3% chord and 90% span with flap phase of 120˚

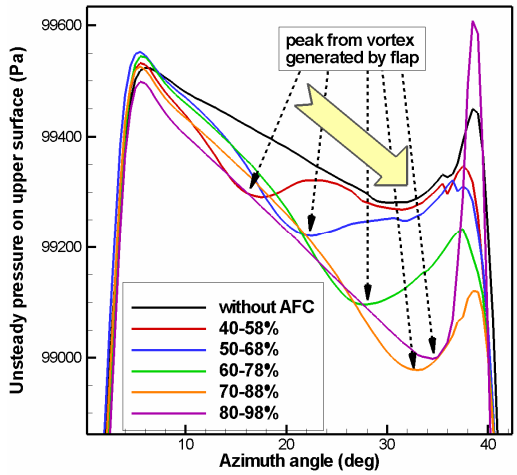

(a) upper surface

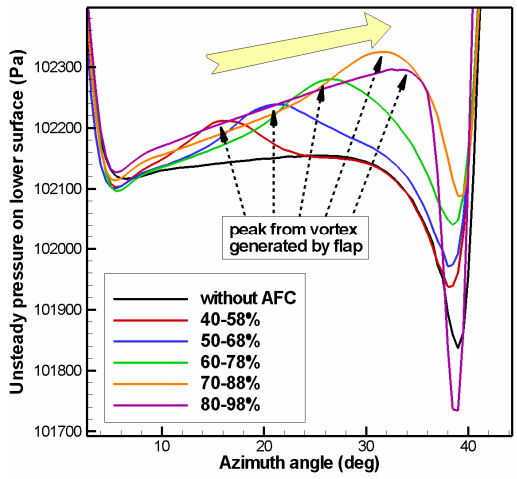

(b) lower surface

Fig. 20: Zoom-view of pressure history at surface point of 3% chord and 90% span with flap phase of 120˚

4.3 Noise Analysis

The changes of surface pressure are converted to the change in BVI noise by noise analysis using aero-acoustic solver at the Microphone position which is shown in Fig.10 and at a far-field position.

Figure 21 visualizes the distribution of peak sound pressure on the hemispherical surface for one of the test calculation. Sound pressure at the far-field position (r=100*R*) for every 5˚ in both azimuth angle and elevated angle are calculated for one revolution, and the peak sound pressure at each position are expressed on the hemisphere surface. From this figure, the noise signal strongly propagates almost downward in the present BVI conditions, where the free-stream velocity and the rotor rotational speed are low.

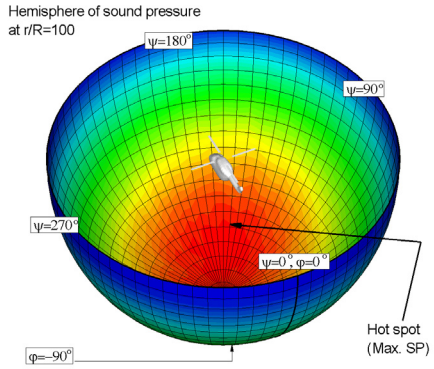

Fig. 21: Directivity of BVI noise in hemisphere of sound pressure at *r/R*=100.

To see the effect of flap position and phase, sound pressure history for one revolution at the position where the sound pressure becomes maximum on the hemisphere at *r/R*=100 is plotted in Fig. 22. The calculated sound pressure waveform of BVI noise clearly shows distinct spikes caused by the interactions between blades and vortices, and the magnitude of peak differs according to the flap condition. As flap moves outward (0.80-0.98*R*), the change of peak sound pressure becomes large. For the case of 0.80-0.98*R,* the peak sound pressure of phase 60˚ is less than the one without AFC, and peak goes up for the case of phase 120˚. On the contrary, for the case of 0.60-0.78*R*, the noise reduction is achieved at the phase 120˚, even the reduction is comparatively small in magnitude.

One more thing to be mentioned is the effect of flap vortex interaction, which is explained in Fig. 20. Compared to the strong peak from BVI, the change of sound pressure by the interaction with flap vortex seems negligible, which implies that the interaction with flap vortex has a minor effect on far-field noise when considering the BVI noise. Also as flap moves inward, the difference in peak sound pressure becomes less. From this result of quantitative comparison, we can guarantee that for the design of inward flap for other purpose such as vibration control, the BVI interference by the flap vortex is negligible.

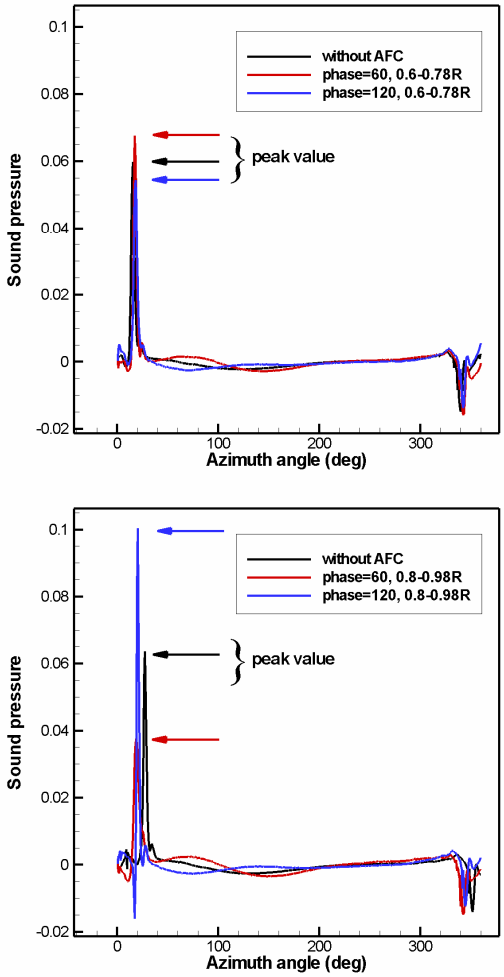

Fig 22: Sound pressure of maximum point on the hemisphere at *r/R*=100.

To see the effect of geometric position of flap more clearly, the peak sound pressure at Mic 1 and far-filed according to the flap beginning position at the several fixed phase angle of flap are shown in Fig. 23.

As the flap moves outward to tip, the amplitude of oscillation becomes larger, which implies bigger effect of AFC onto BVI noise variation. The opposite tendency of sound pressure oscillation between the inner flap (flap beginning around 0.40*R* to 0.60*R*) and the outer flap (flap beginning around 0.70*R* to 0.80*R*), which also described in Fig 22, appears in these figures.

These phenomena is obviously dependent on BVI configuration according to the flight conditions, the discussion should be limited to the present calculating conditions. As one of the explanations, the opposite tendency of sound pressure oscillation is considered from the different mechanism of noise reduction according to the flap position by two most important parameters on BVI noise, miss-distance and vortex strength, which are strongly related to the lift of blade.

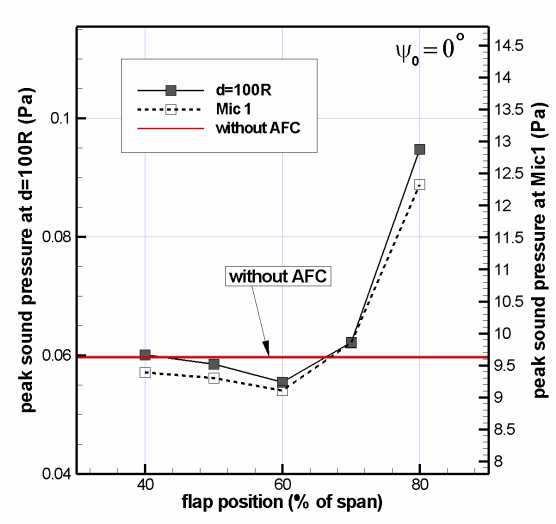

(a) phase=0˚

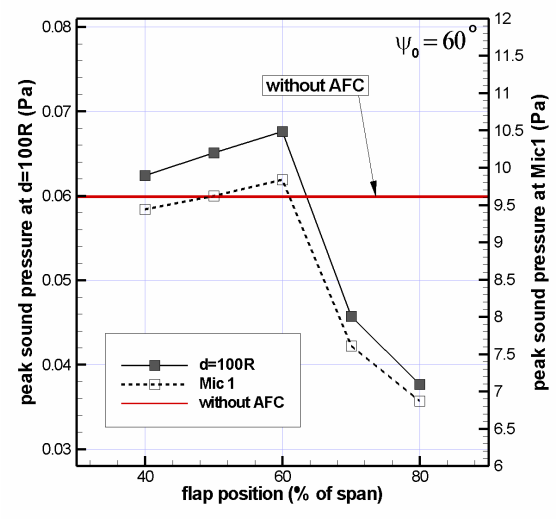

(b) phase=60˚

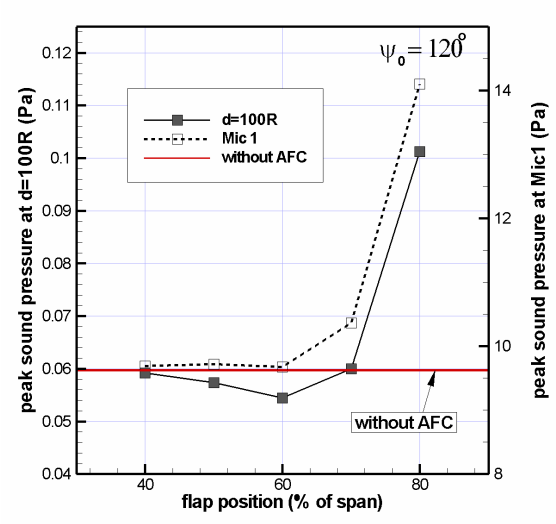

(c) phase=120˚

Fig 23: Peak sound pressure at Mic 1 and far-filed according to the flap position

And the lift of blade varies according to the flap motion with phase and span-wise position. The switch of oscillating patterns for the outward flap and the inward flap are considered from the sensitivity of the effect by miss-distance and vortex strength in opposite ways. As flap moves outward, the lift of blade change rapidly, and the miss-distance increases to reduce the BVI noise and the vortex strength also increases to raise BVI noise. But as explained Fig. 13, the sensitivity of miss-distance is fairly big to play a dominant role in the case of outward flap when the large blade lift produces large miss-distance. As flap moves inward, the effect of miss-distance lose its control power dramatically to leave major role to the vortex strength, even the effect of vortex strength also becomes less.

As flap moves further inward, the effect of both miss-distance and vortex strength becomes negligible to produce rarely difference with the case without AFC, as shown at 40 % of span in Fig. 23. The switch of these two control power seems to occur around the phase between 60˚ and 70˚ as shown at all plots in Fig. 23. Even though more specified calculations are needed to find out more accurate position and the switching mechanism according to the flap position, the present results show a good demonstration for the different pattern of BVI noise reduction by flap position.

Figure 24 shows the variation of peak sound pressure at far-filed according to the phase with fixed span-wise flap position as a concluding graph. Compared to the outer flap(0.80-0.98*R*), the inner flap(0.60-0.78*R*) shows less amplitude, which implies less effect on BVI noise reduction. Also the opposite pattern of upper and lower peak positions shows the switching phenomena explained in Fig. 23.

If we consider the maximum noise reduction by AFC, we can say that the flap should locate outward (near tip region) with the proper condition of well-adjusted phase, which is corresponding to 60˚ of flap phase with flap position of 0.80-0.9*R* in the present calculation condition.

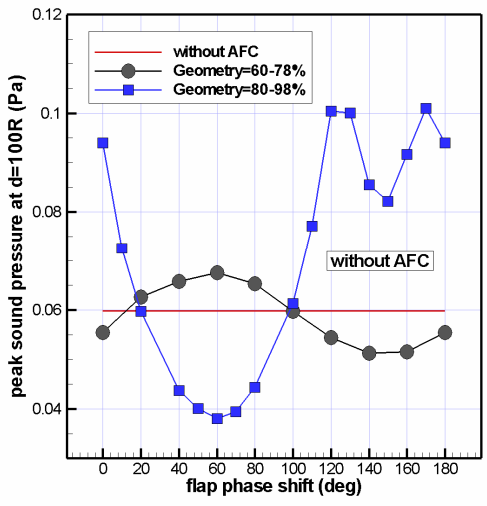

Fig 24: peak sound pressure according to flap phase

5. SUMMARIES

A three-dimensional unsteady Euler code for the analysis of active flap control has been developed based on an advanced CFD code and the effect of position of AFC on BVI noise is analyzed by combining the new CFD code with an acoustic code. As a result, the followings were found.

1. The present method successfully captures the distinct spikes of BVI noise and shows agreement with experimental data. The capability of the present method is also demonstrated to capture the effect of AFC on blade aerodynamics by comparing the change of sound pressure with experimental data.

2. The theoretical and calculated analysis of blade lift for one revolution according to flap condition shows meaningful agreement to understand the effect of flap conditions on the BVI noise.

3. The major effect of AFC is to change the blade lift as a function of flap position and flap phase, and the effect of interaction between blade and flap vortex is negligible on the BVI noise.

4. The effect of flap position on BVI noise is quantitatively predicted to show that the flap near tip region is more effective to achieve BVI noise reduction in the condition of well-adjusted phase.

5. The difference of mechanism between phase control and position control need more discussion to understand the comprehensive effect of AFC on BVI noise.

ACKNOWLEDGMENTS

The authors would like to thank Mr. Noboru Kobiki in JAXA for his discussions and advices.

REFERENCES

[1] Gopalan, G., Schmitz, F. H., and Sim, B. W., Flight Path Management and Control Methodology to Reduce Helicopter Blade-Vortex Interaction (BVI) Noise, AHS Vertical Lift Aircfraft Design Conference, San Francisco, CA, Jan., 2000.

[2] Schmitz, F. H., Gopalan, G., and Sim, B. W., Flight Trajectory Management to Reduce Helicopter Blade-Vortex Interaction (BVI) Noise with Head/Tailwind Effects, 26th ERF, No. 77, The Hague, The Netherlands, Sep., 2000.

[3] Boxwell, D. A. and Schmitz, F. H., Full-Scale Measurements of Blade-Vortex Interaction Noise, Journal of the American Helicopter Society, Vol.27, (4), Oct, 1982, pp.11-27.

[4] Martin, R. M. and Connor, A. B., Wind-Tunnel Acoustic Results of Two Rotor Models with Several Designs, NASA-TM 87698, 1986.

[5] Yu, Y. H., Liu, S. R., Jordan, D. E., Landgrebe, A. J., Lorber, P. F., Pollack, M. J., and Martin, R. M., Aerodynamic and Acoustic Test of a United Technologies Model Scale Rotor at DNW, AHS 46th Annual Forum, May, 1990.

[6] Lowson, M. V., Progress Towards Quieter Civil Helicopters, 17th ERF, No. 59, 1991.

[7] Yu, Y. H., Gmelin, B., Splettstoesser, W., Philippe, J.J., Prieur, J., and Brooks, T., Reduction of Helicopter Blade-Vortex Interaction Noise by Active Rotor Control Technology, Prog. Aerospace Sci., Vol. 33, 1997, pp. 647-687.

[8] Baeder, J. D., Passive Design for Reduction of High-Speed Impulsive Rotor Noise, AHS 52nd Annual Forum, Washington DC, June 1996.

[9] Aoyama, T., Aoki, M., Kondo, N., Saito, S., and Kawachi, K, Effect of Blade-Tip Shape on High-Speed Rotor Noise, AIAA Paper 96-2380, June 1996.

[10] Arnold, U. T. P., Fürst, D., Closed Loop IBC Results from Recent CH-53G Flight Tests, 30th ERF, 2004.

[11] Kobiki, N., et al., Active Tab, a New Active Technique for Helicopter Noise Reduction, 29th ERF, 2003.

[12] Kobiki, N., Akasaka, T., Kondo, N., Tanabe, Y., and Saito, S., An Experimental Study of On-blade Active Tab for helicopter noise reduction, 30th European Rotorcraft Forum, September 2004.

[13] Aoyama, T., Yang, C., Saito, S., Numerical Analysis of BVI Noise Reduction by Active Tab, 60th AHS Annual Forum, 2004.

[14] Riemenschneider, J., Keye, S., Wierach, P., Rochettes, H. M., Review of the Common DLR/ONERA Project “Active Twist Blade” (ATB), 30th ERF, 2004.

[15] Shin, S., Cesnik, C. E. S., Hall, S. R., Closed-loop Control Test of the NASA/Army/MIT Active Twist Rotor for Vibration Reduction, AHS 59th Annual Forum, Phoenix, AZ, May, 2003.

[16] Weems, D. B., Anderson, D. M., Mathew, M. B., Bussom, R. C., A Large-Scale Active-Twist Rotor, AHS 60th Annual Forum, Baltimore, MD, May, 2004.

[17] Booth, E. R., Jr., Wilbur, M. L., Acoustic Aspects of Active-Twist Rotor Control, AHS 58th Annual Forum, Montreal, Canada, June, 2002.

[18] Friedmann, P. P., Vibration Reduction In Rotorcraft Using Actively Controlled Flaps - Their Evolution and Potential for Improving Rotorcraft Technology, 30th ERF, 2004.

[19] Liu, L., Patt, D., and Friedmann, P. P., Simultaneous Vibration and Noise Reduction in Rotorcraft Using Aeroelastic Simulation, 60th AHS Annual Forum, 2004.

[20] Patt, D., Liu, L., and Friedmann, P. P., Achieving Simultaneous Reduction of Rotorcraft Vibration and Noise Reduction Using Simulation, 30th ERF, 2004.
[21] Bernhard, A. P. F., O'Neill, J., Kohlhepp, F., Welsh, W., Lorber, P., Active Rotor Control (ARC) of a Mach-Scale Trailing Edge Flap Rotor, AHS 57th Annual Forum, Washington, DC, May, 2001.
[22] Stevens, P. W., Smith, E. C., Active Interrogation of Helicopter Rotor Faults using Trailing Edge Flap Actuation, AHS 57th Annual Forum, Washington, DC, May, 2001.
[23] Hasegawa, Y., Katayama, N., Kobiki, N., Yamakawa, E., Whirl Test Results of ATIC Full Scale Rotor System, 26th European Rotorcraft Forum, The Hague, The Netherlands, 2000.
[24] Hasegawa, Y., Katayama, N., Kobiki, N., Nakasato, E., Yamakawa, E., Okawa, H., Experimental and Analytical Results of Whirl Tower Test, AHS 57th Annual Forum, Washington, DC, May, 2001.
[25] Fink, D. A., Hawkey, T. J., Gaudreau, M. P. J., Wellman, B., Ormiston, R. A., An Electromagnetic Actuator for Individual Blade Control, AHS 56th Annual Forum, Virginia Beach, VA, May, 2000.
[26] Leconte, P. and Kube, R., Main Rotor Active Flaps: Numerical Assessment of Noise and Vibration Reduction, 2nd DLR-ONERA Aerospace Symposium, 2000.
[27] Enenkl, B., Klöppel, V., Preissler, D., Jänker, P., Full Scale Rotor with Piezoelectric Actuated Blade Flaps, 28th European Rotorcraft Forum, Bristol, UK, 2002.
[28] Toulmay, F., Klöppel, V., Lorin, F., Enenkl, B., Gaffiero, J., Active Blade Flaps – The Needs and Current Capabilities, AHS 57th Annual Forum, Washington, DC, May, 2001.
[29] http://www.boeing.com/news/releases/2004/q2/nr_040518t.html.
[30] Koratkar, N. A., Spencer, M. G., Chopra, I., Wind Tunnel Testing of a Mach-Scaled Active Rotor with Trailing-Edge FLAPS, AHS 57th Annual Forum, Washington, DC, May, 2001.
[31] Chopra, I., Status of Application of Smart Structures Technology to Rotorcraft Systems, J. of AHS, Vol. 45, No. 4, pp. 228-252, 2000.
[32] Milgram, J., Chopra, I., and Straub, F., Rotors with Trailing Edge Flaps: Analysis and Comparison with Experimental Data, J. of AHS, Vol. 43, (4), 1998, pp. 319-332.
[33] Hariharan, N, and Leishman, J. G., Unsteady Aerodynamics of Flapped Airfoil in Subsonic Flow by Indicial Concepts, J. of Aircraft, Vol. 33, (5), Sep.-Oct. 1996, pp. 855-868.
[34] Bagai, A., and Leishman, J. G., Rotor Free-Wake Modeling Using a Pseudo-Implicit Technique Including Comparisons with Experimental Data, J. of AHS, Vol. 40, (3), 1995.
[35] Myrtle, T. F. and Friedmann, P. P., Vibration Reduction in Rotorcraft Using Actively Controlled Trailing Edge Flaps and Issues Related to Practical Implementation, 54th AHS Forum, May, 1998.
[36] Aoyama, T., Yang, C., and Saito, S., Numerical Analysis of Active Flap for Noise Reduction Using Moving Overlapped Grid Method, AHS 61st Annual Forum, May, 2005.
[37] Yang, C., Aoyama, T, Saito, S., Numerical Analysis of Interaction Noise between Main Rotor and Tail Rotor of Helicopter, 24th ICAS, Yokohama, August, 2004.
[38] Boxwell, D. A. and Schmitz, F. H., Full-Scale Measurements of Blade-Vortex Interaction Noise, Journal of the American Helicopter Society, Vol.27, (4), Oct, 1982, pp.11-27.
[39] Aoyama, T., Kawachi, K., Saito, S., Unsteady Calculation for Flow-field of Helicopter Rotor with Various Tip Shapes, 18th European Rotorcraft Forum, Paper No.B03, Avignon, France, September 1992.
[40] Yamamoto, S. and Daiguji, H., Higher-Order-Accurate Upwind Schemes for Solving the Compressible Euler and Navier-Stokes Equations, J. of Computers & Fluids, 22, pp.259-270, 1993.
[41] Shima, E. and Jounouchi, T., Role of CFD in Aeronautical Engineering (No.14) - AUSM type Upwind Schemes -, NAL SP-34, 1999, pp. 7-12.
[42] Nakamura, Y., and Azuma, A., "Rotational Noise of Helicopter Rotors," Vertica, vol. 3, No. 3/4, pp.293-316, 1979.
[43] Farassat, F., Theory of noise generation from moving bodies with an application to helicopter rotors, NASA TR R 451, 1975.
[44] Strawn, R. C., Duque, E. P. N., Ahmad, J., Rotorcraft Aeroacoustics Computations with Overset-Grid CFD Methods, Journal of AHS, Vol. 44, No. 2, 1999, pp. 132-140.
[45] Kobiki, N., Tsuchihashi, A., Murashige, A., Yamakawa, E., Elementary Study for the Effect of HHC and Active Flap on Blade Vortex Interaction, 23rd European Rotorcraft Forum, Dresden, Germany, September, 1997.